Journal of Alloys and Compounds 815 (2020) 152417

Contents lists available at ScienceDirect

Journal of Alloys and Compounds

journal homepage: http://www.elsevier.com/locate/jalcom

Predictions of long-term creep life for the family of 9–12 wt% **Cr** martensitic steels

Amit K. Verma [a], Jeffrey A. Hawk [b], Vyacheslav Romanov [c], Jennifer L.W. Carter [a, *]

[a] Department of Material Science and Engineering, Case Western Reserve University, Cleveland, OH, 44106, USA
[b] National Energy Technology Laboratory, Albany, OR, 97321-2198, USA
[c] National Energy Technology Laboratory, Pittsburgh, PA, 15236-0940, USA

ARTICLE INFO

Article history:
Received 8 July 2019
Received in revised form
20 September 2019
Accepted 23 September 2019
Available online 1 October 2019

Keywords:
Creep power law
Accelerated testing
Martensitic steels
Metal design

ABSTRACT

Two contemporary power-law creep methodologies for predicting long-term creep life from short-term lab-based experiments were extended to 48 different alloy compositions in the family of 9–12 wt% **Cr** steels. The study highlights the limitations that the data imposes on the applicability of the two methods for predicting lifetimes, while also assessing the assumptions made by both methods. It was found that a dependency exists between the creep activation energy and the test conditions when activation energy was calculated using a broader range of normalized stress states (σ/σ_{TS}) than were previously explored. This contradicts the assumptions of constant activation energy made by both contemporary methods. This raises questions about both the physical interpretation of activation energy and the reliability of the extrapolation of lifetime predictions made. The paper highlights that the modified power-laws are empirical tools and illustrates the importance of study protocol design for data collection, when short-term experiments are limited to a maximum of 6,000 h. In addition, the effects of alloying additions and tempering temperature on the creep mechanism were explored.

1. Introduction

With the rapidly changing landscape of electricity generation [1], it is imperative that advanced ultra-supercritical (A-USC) power plants be adopted, with increased steam temperature and lower carbon dioxide (CO_2) emissions [2]. New materials are needed for various component applications such as turbine and boiler components to withstand the more severe service conditions. Under the proposed A-USC standards [2], 9–12 wt% **Cr** class of martensitic steels are being considered for thick sections such as the main steam pipe and header in the boiler to operate up to 650 °C and above, with a minimum creep lifetime of 30 years (~ 263,000 h). Due to extended time-frames, multiple numerical methods [3,4] and their subsequent versions [5,6] have attempted to reduce the maximum test duration needed to qualify the lifetime properties for the design of new materials. However, multiple uncertainties [7] have led to overestimation of long term performance, emphasizing the limitations of numerical methods [3–6] and have justified the completion of long-term tests. New methods such as proposed by Wilshire et al. [8] and Zhao et al. [9] have shown an ability to reduce this test time-frame and provide reasonable estimates of long creep lifetimes for a variety of material systems (i.e., aluminum alloys, nickel alloys, etc.) using short term tests lasting only 5,000 h and 6,000 h, respectively. Therefore, these methodologies have the potential to accelerate the design process and allow an early transition to A-USC power plants. In this paper, both methodologies have been applied to 48 different creep-resistant alloys from the MatNavi database provided by National Institute for Materials Science (NIMS), Japan [10–18], and an attempt has been made to identify the effect of alloying elements on long-term creep behavior.

2. Methods

Both methods [8,9] follow a similar approach with minor differences. The approach can be dissected into three steps: (1) establishing a relationship between minimum creep rate ($\dot{\varepsilon}_{min}$) and creep rupture time (t_f) (2.1); (2) calculation of activation energy (Q) using modified power law (2.2); and (3) predicting strength using modified power law (2.2).

* Corresponding author.
E-mail address: jennifer.w.carter@case.edu (J.L.W. Carter).

https://doi.org/10.1016/j.jallcom.2019.152417
0925-8388/

2.1. Dependency of $\dot{\varepsilon}_{min} \sim t_f$

Creep life (t_f (sec)) is inversely related to the minimum creep strain rate ($\dot{\varepsilon}_{min}$ (1/sec)) through the Monkman-Grant relationship [19]. The relationship can be written as:

$$\dot{\varepsilon}_{min} = M t_f^{-m} \text{ or } \ln \dot{\varepsilon}_{min} = \ln M - m \ln t_f \quad (1)$$

where M and m are material constants independent of test conditions. However, Wilshire et al. [8] assumed m as equal to 1, while, Zhao et al. [9] calculated m using the above linear relationship between ln ($\dot{\varepsilon}_{min}$) and ln (t_f). This minor difference results in restrictions on the databases used for the two methods, as the calculation of m/M requires pairs of $\dot{\varepsilon}_{min}$, t_f values exist in the dataset. Alternatively, assuming m is equal to 1 eliminates this necessary condition and allows subsequent calculations with either one of the available variable.

2.2. Modified power law

Conventionally, the functional relationship between $\dot{\varepsilon}_{min}$ and t_f with applied stress (σ) and test temperature (T) for dislocation-mediated creep mechanism is quantified by using the creep power law [20] of the form:

$$\dot{\varepsilon}_{min} = M t_f^{-m} = A\, \sigma^n \exp\left(-Q_c / RT\right) \quad (2)$$

where R is the universal gas constant (8.314 J mol^{-1} K^{-1}), A is a proportionality constant, n is the stress exponent, and Q_c is the activation energy of creep. The fundamental assumption of the power-law model is that a steady-state creep rate exists, consistent with a balance between deformation and recovery mechanisms, creating a constant microstructure. This is not the observed case for the creep rates of many material systems in which both n and Q_c are dependent on σ and T. Thus it is difficult to use the above form for understanding physical mechanisms or the prediction of long-term strength using short-term data. To rectify this issue, Wilshire et al. [8] normalized the applied stress (σ) with the ultimate tensile strength (σ_{TS}) measured at creep test temperature, transforming the power law to:

$$\dot{\varepsilon}_{min} = M t_f^{-1} = A^* \left(\sigma/\sigma_{TS}\right)^n \exp\left(-Q_c^* / RT\right) \quad (3)$$

where $A^* \neq A$ and $Q_c^* \neq Q_c$. In this case, Q_c^* was determined using Equation (3) for a constant value of σ/σ_{TS}. This accounts for the change in Q_c values found with Equation (2), although it does not eliminate the gradual decrease in n with decreasing σ. To account for changes in n, Wilshire et al. [8] proposed a second functional relationship:

$$\sigma \Big/ \sigma_{TS} = \exp\left\{ - k_1 \left[t_f \exp\left(- Q_c^* / RT\right)\right]^u \right\} \quad (4)$$

where k_1 (intercept) and u (slope) are evaluated from plots of $\ln[t_f \exp(-Q_c^*/RT)]$ against $\ln[-\ln(\sigma/\sigma_{TS})]$, using calculated Q_c^* from Equation (3). Note: an exponential of $\{A^*/M\,[t_f\,(-Q_c^*/RT)]\}^{1/n}$ was taken in Equation (3) to reach Equation (4). This replaces the gradual changing value of n with σ/σ_{TS}, with an almost constant albeit piecewise linear change in u with σ/σ_{TS}.

Zhao et al. [9] modified the power law to:

$$\dot{\varepsilon}_{min} = M t_f^{-m} = A^{'} \left[\sigma/(\sigma_{TS} - \sigma)\right]^n \exp\left(-Q_c^{'} / RT\right) \quad (5)$$

where $Q_c^{'}$ was determined at a constant value of $\sigma/\ \sigma_{TS}$. The difference between Q_c^* and Q'_c, and the role of m will become clear in the subsection 4.3. For predictions of creep life for an applied stress or vice versa, using short-term data, Zhao et al. [9] rearranged the Equation (5) to:

$$\ln\left\{\dot{\varepsilon}_{min} \exp\left(Q_c^{'} / RT\right)\right\} = \ln A^{'} + n \ln[\sigma / (\sigma_{TS} - \sigma)] \quad (6)$$

Using the calculated $Q_c^{'}$, left hand side of Equation (6) can be calculated for different σ and T, and when plotted against $\ln[\sigma/(\sigma_{TS} - \sigma)]$ all data fall on a piecewise linear function providing the slope (n) and the intercept (A'). This methodology resolves the dependency of both n and Q_c on σ/T in a single step, and changes the relationship between n and σ/σ_{TS} to a piecewise linear function while making Q'_c independent of σ/T.

3. Data science methods

3.1. Change-point detection

A change-point is coordinated where two different linear relationships (i.e., with different slopes) between the same pair of variables converge. In materials science, for example, these change-points could signify a change in the dominant deformation or microstructural evolution mechanism. The **R** segmented package [21] uses maximum likelihood to fit a piecewise model where the method constrains the linear segments to be (nearly) continuous [22]. The function takes a generic linear model and a starting value(s) of the change-point(s) (a best-guess estimate) as its arguments, and iteratively varies these parameters to get the best fit by minimizing the gap between the segments. For the methods employed, change-points were calculated to determine the associated changes in k_1, u, and n values with σ/σ_{TS}.

3.2. Measure of fitness

To evaluate the performance of the methods, a measure of fitness needs to be defined to quantify how well the predictions match the observed data. The most commonly-used measure is the mean squared error (MSE) [23], given by:

$$MSE = \frac{1}{n}\sum_{i=1}^{n} (y_i - \hat{f}(x_i))^2 \quad (7)$$

where $\hat{f}(x_i)$ is the prediction that $\hat{f}$ (model) gives for the i_{th} observation. The MSE will be small if the predicted responses are very close to the true responses, and will be large if the predicted and true responses differ substantially. One derivative of MSE is root mean squared error (or RMSE), which is just the square root of MSE. The square root is introduced to make the scale of the errors the same as the scale of targets. RMSE is always non-negative, and a value of 0 would indicate a perfect fit. The effect of each error on RMSE is proportional to the size of squared error, thus large errors have a disproportionately large effect, which makes RMSE sensitive to outliers.

RMSE is scale-dependent, therefore, it can be used to compare two different models for a particular dataset, although it cannot be used to compare models between two different datasets. Also, the absolute value of RMSE does not indicate the extent to which the model fits the data. The R^2 statistic [23] provides an alternate measure of fit, which takes the form of a proportion, and it takes on a value between $-\infty$ and 1, and is scale-independent. The formula to calculate R^2 is

$$R^2 = 1 - \frac{MSE(model)}{MSE(baseline)} \quad (8)$$

where MSE (model) is computed using Equation (7), while MSE

(baseline) is defined as

$$MSE(baseline) = \frac{1}{n}\sum_{i=1}^{n}(y_i - \bar{y})^2 \quad (9)$$

where $\bar{y}$ is the mean of the observed y_i. MSE (baseline) measures the total variance in response *Y*, and can be thought of as the MSE that the simplest model would get, where simplest possible model would always predict the average of all samples. A value close to 1 indicates a model with close to zero error, a value close to zero indicates a model very close to the baseline, and a negative value indicates a model worse than the baseline model. For this study, both RMSE and R^2 values are provided to reflect the performance of methods.

4. Results and analysis

The dataset contains creep test results ($\dot{\varepsilon}_{min}$, t_f) for different test environments (σ, *T*) and processing parameters such as composition and heat treatment. The compositional space comprises of 48 unique combinations of 18 different elements. The alloy specifications (tabulated in Table 1) ensure a fully tempered martensitic microstructure by balancing the austenite and ferrite stabilizers. Within the 9–12 wt% **Cr** class of martensitic steels, the 10 alloy subclass labels were assigned by following the naming conventions [24]. The dataset contains a total of 1621 observations of creep performance (888 $\dot{\varepsilon}_{min}$, 1576 t_f), along with temperature specific tensile strength values (σ_{TS}) determined by uniaxial testing.

4.1. Data availability ($\dot{\varepsilon}_{min}$, t_f)

Of the 1621 creep tests, 843 tests reported both $\dot{\varepsilon}_{min}$ and t_f (Fig. 1). For the remaining data, 733 tests reported only t_f and 45 tests reported only $\dot{\varepsilon}_{min}$. The missing values of $\dot{\varepsilon}_{min}$ and t_f play a role in selection of one methodology over the another (as discussed in section 2.1). For example, 788 tests where $\dot{\varepsilon}_{min}$ or t_f are missing does not affect the Wilshire methodology [8] as it only needs one of the two variables for all the calculations. For the Zhao methodology [9], the evaluation of *m* needs a sufficient number of ($\dot{\varepsilon}_{min}$, t_f) pairs for a linear fit of Equation (1) for each unique alloy composition. This eliminates 13 unique compositions, a total of 353 observations, where creep performance data only has t_f values. Further, putting a threshold of a minimum of six ($\dot{\varepsilon}_{min}$, t_f) pairs for a linear fit (Equation (1)) eliminates three more unique compositions, 76 observations. For the 32 remaining compositions in which a sufficient number of ($\dot{\varepsilon}_{min}$, t_f) pairs exist to calculate *m*, the $\dot{\varepsilon}_{min}$ / t_f missing values were calculated from the other using the Monkman-Grant relationship [19] (Equation (1)) (Fig. 2). This results in 1192 observations that can be used for modeling using the Zhao methodology.

4.2. Wilshire method: calculation of Q_c^*

Rearranging Equation (3) gives:

$$\ln t_f = Q_c^* \Big/ RT - n\ln(\sigma / \sigma_{TS}) + \ln(M / A^*) \quad (3')$$

Using above form, Q_c^* is calculated from a linear fit between $\ln(t_f)$ and $1/T$ at approximately same σ/σ_{TS}. Fig. 3 shows a histogram of σ/σ_{TS} for a single composition from **9Cr–Mo-1.8W–V–Nb–B** (■) sub-class, highlighting that multiple measurements can be made for Q_c^* for different intervals of σ/σ_{TS}. Therefore, for an unbiased estimation, Q_c^* must be evaluated for different σ/σ_{TS} values with varying interval widths. It should be noted that the stress exponent *n* decreases with decrease in σ/σ_{TS} [8] and may affect Q_c^* values,

Table 1
Composition and heat treatment ranges for the alloy sub-classes of the class of 9–12 wt% Cr martensitic steels used in the analysis. The main alloying additions are shown with units in wt%. Elements such as Si, Al, P, N, S, and the remaining Fe content are not included. Heat treatment temperature ranges are presented as TPR for tempering temperature (°C), and NML for normalization temperature (°C). NA represents that some of the observations within the sub-class did not contain the element.

	Sub-Class	C	Cr	Mn	Ni	Mo	W	Co	Cu	Nb	V	B	NML	TPR
(△)	12Cr	0.12–0.14	11.64–12.38	0.42–0.71	0.15–0.45	0.04–0.21			0.03–0.21				950–980	630–750
(◇)	9Cr–1Mo	0.09–0.13	8.46–9.15	0.38–0.50	0.047–0.120	0.93–1.05			0.02–0.08				900–970	720–860
(⊞)	9Cr–2Mo	0.05	9.04	0.5	0.11	2.03			0.02	0.006	0.01		950	800
(□)	9Cr-1.5Mo-1.3Co–V–Nb–B	0.12–0.14	9.28–9.31	0.31–0.34	0.15	1.51–1.54	0.005 (NA)	1.25–1.33	0.02 (NA)	0.050–0.052	0.19–0.20	0.0091–0.0096	1095–1100	660–700
(○)	10.5Cr–1Mo–1W–V–Nb	0.12–0.15	9.94–10.44	0.41–0.55	0.67–0.79	0.97–1.10	0.97–1.00	0.02 (NA)		0.040–0.050	0.17–0.20		1050	650–690
(▽)	12Cr–1Mo–1W–Co–V–Cu	0.19–0.25	11.00–12.90	0.55–0.87	0.64–0.90	0.91–1.22	0.90–1.13	0.04–0.15	0.03–0.15		0.21–0.30		1030–1050	630–660
(⊕)	9Cr–1Mo–V–Nb	0.08–0.11	8.31–8.74	0.35–0.49	0.04–0.28	0.89–0.99			0.012–0.032 (NA)	0.048–0.09	0.185–0.23		1045–1060	760–790
(■)	9Cr–Mo-1.8W–V–Nb–B	0.098–0.11	9.26–9.50	0.41–0.42	0.13–0.17	0.36–0.42	1.67–1.74			0.057–0.062	0.16–0.19	0.002	1070–1100	780
(•)	10.5Cr–Mo–2W–V–Nb–Cu–B	0.12–0.13	10.65–10.73	0.60–0.63	0.32–0.36	0.33–0.38	1.87–1.97		0.85–0.97	0.050–0.056	0.19–0.22	0.0024–0.0039	1050	770
(▲)	12Cr–Mo-1.8W–V–Nb–Cu–B	0.11	12.10	0.59	0.33	0.34	1.82		0.82	0.06	0.19	0.003	1050	790

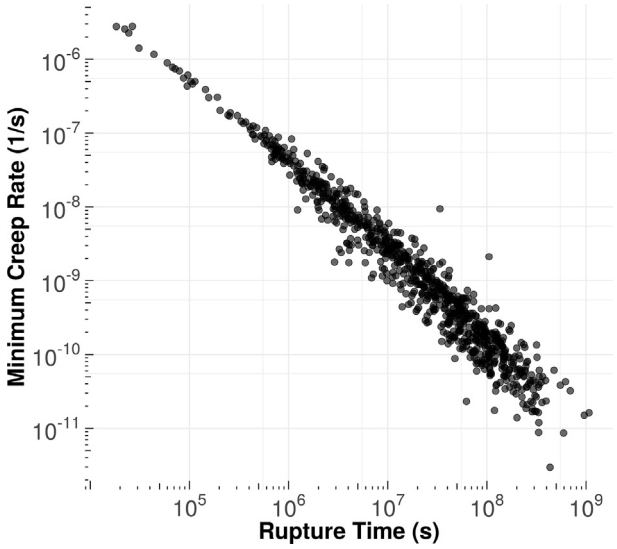

Fig. 1. Visualization of minimum creep rate with creep rupture time for a total of 843 observations show an inverse relationship with few outliers.

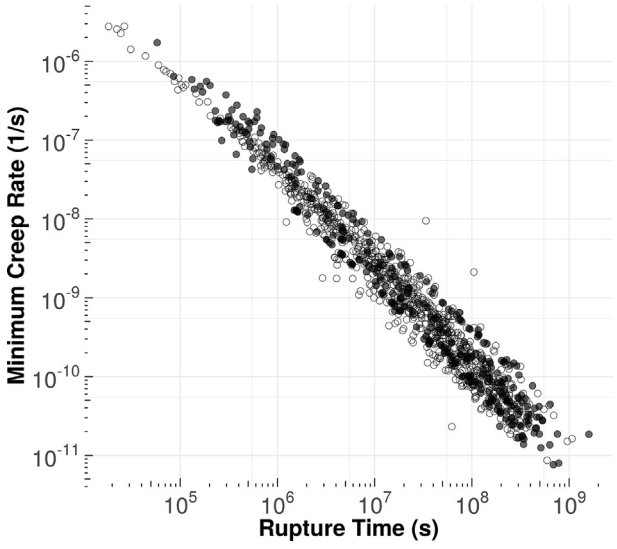

Fig. 2. Visualization of minimum creep rate with creep rupture time for a total of 1192 observations, where closed circles correspond to 366 observations where either $\dot{\varepsilon}_{min}$ / t_f were calculated from the other using the Monkman-Grant relationship, while open circles correspond to the experimental data previously presented in Fig. 1.

although, Wilshire et al. stated otherwise. Thus, the above approach may highlight these dependencies too.

A R-language [25] function (Appendix A) was written to divide the data into intervals of varying widths and Q_c^* was calculated for each interval. The function iteratively performs three steps: (1) divide the data into fixed intervals of σ/σ_{TS}, (2) take each interval and fit a linear function between $\ln(t_f)$ and $1/T$, and (3) evaluate Q_c^* using slope of the fit. At each iteration, the σ/σ_{TS} interval width increases, where the minimum and maximum width of the intervals are determined by the total number of available $\sigma/\ \sigma_{TS}$ observations and the range of σ/σ_{TS} for an unique composition. The function constrains the fit between $\ln(t_f)$ and $1/T$ in three ways: (1) a minimum of three observations are required, (2) observations must span a minimum of three different temperatures, and (3) the resulting fit should have a minimum R^2 value of 0.90. The iterative

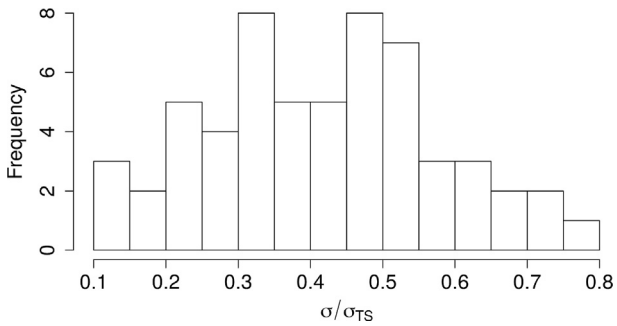

Fig. 3. Histogram of σ/σ_{TS} for an unique composition from **9Cr–Mo-1.8W–V–Nb–B** (■) sub-class.

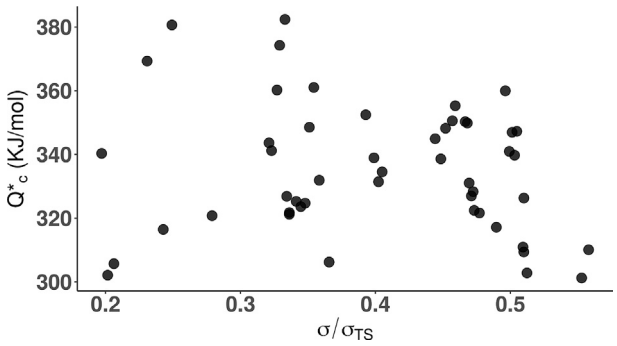

Fig. 4. Visualization of Q_c^* as a function of σ/σ_{TS} for the same unique composition presented in Fig. 3 from the **9Cr–Mo-1.8W–V–Nb–B** (■) sub-class. The mean value of Q_c^* was calculated to be 335 ± 21 kJ/mol.

cycle generates a distribution of Q_c^* for all the tested intervals, where extreme values (± 2*SD away) are eliminated using a normal distribution fitted for maximum goodness-of-fit estimation [26]. Fig. 4 shows the results of the algorithm for a single composition from **9Cr–Mo-1.8W–V–Nb–B** (■) sub-class as a function of σ/σ_{TS}, highlighting that there is no strong dependence of Q_c^* on σ/σ_{TS}. The mean value of Q_c^* was calculated to be $335\pm21 KJ/mol$. This method was subsequently extended to all the available compositions to test the assumption that there is no strong dependence of Q_c^* on σ/σ_{TS}.

4.3. Zhao method: calculation of Q'$_c$

The approach to calculate Q'$_c$ follows the same steps as developed for Q_c^* in subsection 4.2. Instead of Equation (3), here Equation (5) was used with $\dot{\varepsilon}_{min}$ values. Taking the natural-log (ln) on both sides of Equation (5) gives

$$\ln \dot{\varepsilon}_{min} = \ln A' + n \ln [\sigma / (\sigma_{TS} - \sigma)] - Q'_c / RT \quad (5')$$

On calculating the Q'$_c$ value for the same dataset as in subsection 4.2, the mean value of Q'$_c$ was 390 ± 31 kJ/mol. Zhao et al. [9] asserted that Q'$_c$ is independent of σ/σ_{TS} for the modified power law (Equation (5)), when evaluated for a narrow range of σ/σ_{TS}: 0.30–0.45. In this narrow range we observe a similar trend for **9Cr–Mo-1.8W–V–Nb–B** (■) sub-class, although on extending the range (Fig. 5), we found a parabolic dependence between Q'$_c$ and σ/σ_{TS} (R^2 of 0.45).

The difference between the mean values of Q'$_c$ and Q_c^* arises from the assumptions the two methods impose on the value of m (in Equation (1)). An approximate relationship is observed between Q'$_c$ and Q_c^* as:

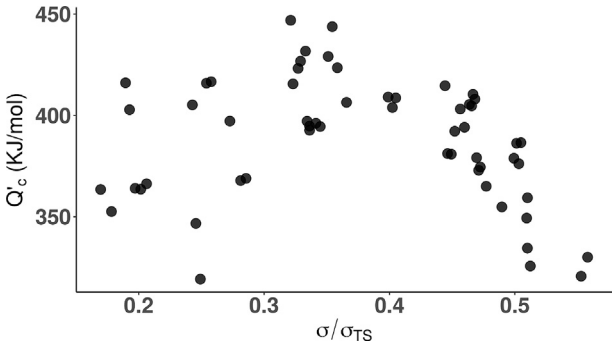

Fig. 5. Visualization of Q'_c as a function of σ/σ_{TS} for the same unique composition as presented in Fig. 4) from the **9Cr–Mo-1.8W–V–Nb–B** (■) sub-class. The mean value of Q'_c is 390 ± 31 kJ/mol.

$$Q'_c / m \approx Q_c^*/1 \text{ or } Q'_c \approx m\, Q_c^* \quad (10)$$

For example, m is 1.142 for the above discussed composition, which makes $Q'_c/m = 341$, close to the Q_c^* (335) calculated in subsection 4.2, highlighting the effect of m on the evaluation of Q_c. The method was extended to all of the available compositions. The mean calculated values for the available data are summarized in Table 2, subsetted with respect to sub-classes, and a comparison of mean values (Q_c^* with Q'_c/m) is shown in Fig. 6.

4.4. Wilshire method: predictions

To assess the effectiveness of the Wilshire method, the model was trained with the dataset where $t_f < 6{,}000$ h, while the model was tested on the dataset where $t_f > 6{,}000$ h. For prediction, k_1 and u were evaluated using Equation (4) and visualized by plotting $\ln[t_f \exp(-Q_c^*/RT)]$ against $\ln[-\ln(\sigma/\sigma_{TS})]$. Change-point detection was used to further separate the training dataset into low vs high σ/σ_{TS} regions (Fig. 7), and subsequently, re-evaluation of k_1 and u was done for respective regions. For validation, a comparison of the predicted versus actual creep rupture strength for the test dataset is visualized in Fig. 8, where fit between the predicted and actual values has a RMSE value of 2.39 and a R^2 value of 0.999.

4.5. Zhao method: predictions

Similarly, to assess the effectiveness of the Zhao method, the model was trained with a dataset where $t_f < 6{,}000$ h, while model was tested on the dataset where $t_f > 6{,}000$ h. The plotting of $\ln\{\dot{\varepsilon}_{min} \exp(Q'_c/RT)\}$ against $\ln[\sigma/(\sigma_{TS}-\sigma)]$ provides the necessary coefficients (slope, n and intercept, A') needed for predictions (Equation (6)). Fig. 9 highlights that the trends in the data is

Table 2
Comparison of Q_c^*, Q'_c, and Q'_c/m mean values for different sub-classes.

	Sub-Class	Q_c^*	Q'_c/m	Q'_c
(△)	12Cr	226–315	231–315	283–363
(⋄)	9Cr–1Mo	205–254		
(⊞)	9Cr–2Mo	340		
(□)	9Cr-1.5Mo-1.3Co–V–Nb–B	353	340	400
(○)	10.5Cr–1Mo–1W–V–Nb	297	299	399
(▽)	12Cr–1Mo–1W–Co–V–Cu	245–349	229–304	290–389
(⊕)	9Cr–1Mo–V–Nb	313–404	307–414	369–457
(■)	9Cr–Mo-1.8W–V–Nb–B	335–340	341	390
(•)	10.5Cr–Mo–2W–V–Nb–Cu–B	246–263	257–273	318–332
(▲)	12Cr–Mo-1.8W–V–Nb–Cu–B	248	245	313

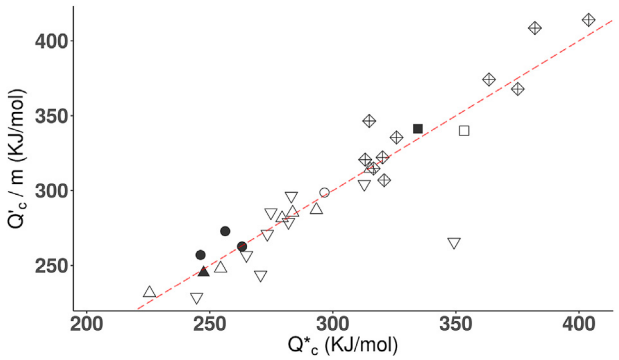

Fig. 6. Visualization of the mean Q_c^* with mean Q'_c/m values for all (32) unique compositions where both values are available. The dashed red line indicates a slope of 1. Different shapes represent sub-classes from Table 2. (For interpretation of the references to colour in this figure legend, the reader is referred to the Web version of this article.)

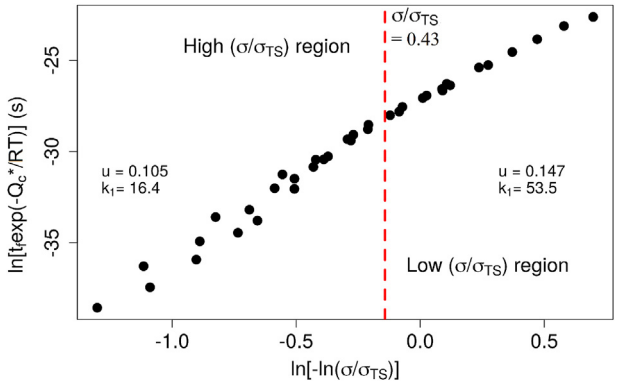

Fig. 7. Visualization of $\ln[t_f \exp(-Q_c^*/RT)]$ verses $\ln[-\ln(\sigma/\sigma_{TS})]$ for the training dataset of the same unique composition as presented in Fig. 3 and 4 from the **9Cr–Mo-1.8W–V–Nb–B** (■) sub-class. The vertical dashed line ($\sigma/\sigma_{TS} = 0.43$) indicates the separation between high and low σ/σ_{TS} regions as calculated using change point detection to solve for the u (slope) and k_1 (intercept) in the two regions.

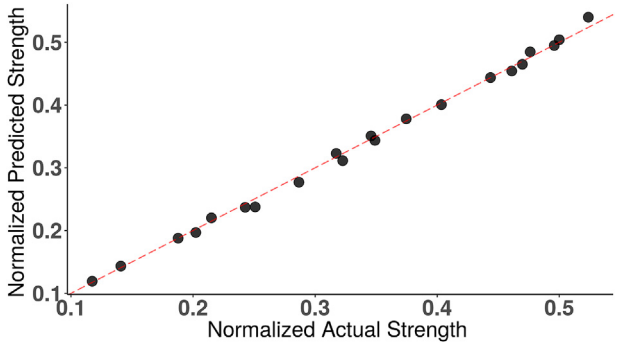

Fig. 8. Visualization of predicted creep rupture strength using Wilshire et al. [8] method against actual strength (both normalized with ultimate tensile strength (σ_{TS})) for the test dataset of the same composition as used for Fig. 7 from **9Cr–Mo-1.8W–V–Nb–B** (■) sub-class. The dashed red line indicates a slope of 1. (For interpretation of the references to colour in this figure legend, the reader is referred to the Web version of this article.)

described by three straight lines with different slopes, however, the third interval ($\ln[\sigma/(\sigma_{TS}-\sigma)] > 0.40$) with slope, $n = 7.27$ can be merged with second interval without a significant change in the predictive capabilities of the functional relationships. There are striking similarities between Figs. 7 and 9, for example, the change-

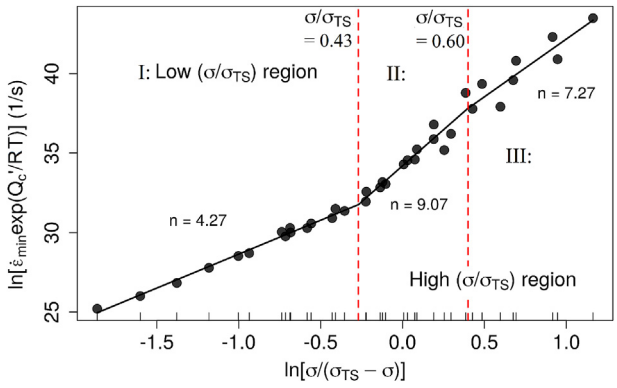

Fig. 9. Visualization of $\ln\{\dot{\varepsilon}_{min}\exp(Q'_c/RT)\}$ against $\ln[\sigma/(\sigma_{TS}-\sigma)]$ for an unique composition (same as Fig. 3/Fig. 4) from **9Cr–Mo-1.8W–V–Nb–B** (■) sub-class. Vertical dashed lines indicate where change in n occur with $\sigma/(\sigma_{TS}-\sigma)$. The inner tick-marks represent the projection of each data point onto the x-axis.

point for Fig. 7 and the first change-point for Fig. 9 ($\ln[\sigma/(\sigma_{TS}-\sigma)] = -0.27$) show up at the equivalent σ/σ_{TS} value of 0.43. Similarly, a comparison of predicted versus actual creep rupture strength for the test dataset is visualized in Fig. 10, where fit between predicted and actual values has a RMSE value of 3.79 and a R^2 value of 0.997. There is no data in the test dataset from the third interval ($\sigma/\sigma_{TS} > 0.60$)(Fig. 10) because this high σ/σ_{TS} range results in short creep lifetimes ($t_f < 6{,}000$ h).

4.6. Predictions: all compositions

On extending the Wilshire methodology to all compositions where Q_c^* was calculated in subsection 4.2 (48 unique compositions), 36 compositions showed a good fit with a RMSE of 7.22 and a R^2 of 0.991. The remaining twelve compositions comprises two types of outliers: (1) two unique compositions where no change-point is calculated within the σ/σ_{TS} range and (2) ten unique compositions, where nine of ten are members of the **12Cr–1Mo–1W–Co–V–Cu** (▽) sub-class, which show high error. The two unique compositions which showed no change-point were considered without the change-point and the results were subsequently added, where linear fits had a R^2 of 0.996 and 0.999, respectively. The second type of outliers is addressed in subsequent subsection 4.7.

For the Zhao methodology, two separate calculations were done: first, with a single change-point; second, with 2 change-points (similar to Fig. 9). The single change-point calculation was done to check if there is any significant difference in RMSE/R^2 value for predictions when considering a single change-point. On extending the Zhao methodology using only single change-point to all the compositions where Q'_c was calculated in subsection 4.3 (32 unique compositions), ten unique compositions showed high error. These ten compositions were the same compositions which showed high error for the Wilshire method. The two unique compositions that show no change-point for Wilshire method, did show a change-point for the Zhao method. This is the result of generating ($\dot{\varepsilon}_{min}$, t_f) pairs for Zhao method using Monkman-Grant relationship [19].

Further, using two change-points, an additional five unique compositions were identified as outliers. The observations of creep performance for these five compositions do not cover a sufficiently large σ/σ_{TS} range to have two change-points, therefore, results with the single change-point were considered. Table 3 sums up the fit results for test data for all the compositions where different methods worked and indicates that there is no significant difference in RMSE/R^2 values for different methodologies.

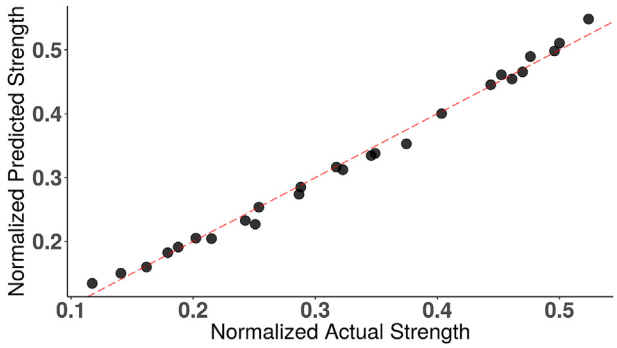

Fig. 10. Visualization of predicted creep rupture strength against actual strength (both normalized with ultimate tensile strength (σ_{TS})) for the same composition as used for Fig. 9 from **9Cr–Mo-1.8W–V–Nb–B** (■) sub-class using Zhao et al. [9] method.

4.7. Outliers

Subsection 4.6 identified the two different classes of outliers. One class of outliers arises because the data did not have sufficient range to exhibit the expected change points in the models. The other class of outliers exhibited high error for all methods, where 9 of 10 unique compositions comprises the **12Cr–1Mo–1W–Co–V–Cu** (▽) sub-class, and is elaborated further. The visualization of $\ln[t_f\exp(-Q_c^*/RT)]$ against $\ln[-\ln(\sigma/\sigma_{TS})]$ for an unique composition from **12Cr–1Mo–1W–Co–V–Cu** (▽) sub-class (Fig. 11) highlights that the training data (open symbols) fall on the piecewise linear fit (line), although there is an imperceptibly small mismatch between the fit and the data points as a function of test temperature. This mismatch is exacerbated for the test dataset (closed symbols) (Fig. 11), which may be attributed to the limited data available for training of piecewise fit (only 11 observations). This is also observed for the rest of the compositions within the **12Cr–1Mo–1W–Co–V–Cu** (▽) sub-class for both methods (Zhao method not visualized, but observed). The other outlier which exhibited high error belong to **9Cr–1Mo–V–Nb** (⊕) sub-class, where multiple observations were collected at similar test conditions (σ/σ_{TS}, T) with different t_f / $\dot{\varepsilon}_{min}$ values, making it difficult for the algorithm to select a change-point.

5. Discussion

5.1. Data limitations

The existence of change points highlights the limitations of data for extrapolation. For example, training data presented in Fig. 7/Fig. 9 covers the σ/σ_{TS} range from 0.134 to 0.762. While test data, limited to observations where $t_f > 6{,}000$ h, has a range of

Table 3
Comparison of different methodologies applied for all possible compositions. *Total* represents the total number of available unique compositions, while *Worked* represents the total number of unique compositions for which the respective methodology worked. **RMSE** represents root mean square error.

Method	Total	Worked	RMSE	R^2
Wilshire	48	38	7.25	0.991
Zhao: 1 change-point	32	22	7.66	0.989
Zhao: 2 change-points	32	17	7.06	0.990

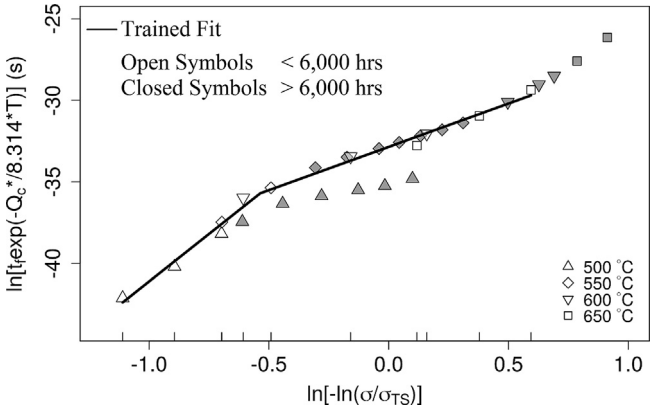

Fig. 11. Visualization of $\ln[t_f \exp(-Q_c^*/RT)]$ against $\ln[-\ln(\sigma/\sigma_{TS})]$ for an unique composition from **12Cr–1Mo–1W–Co–V–Cu** (▽) sub-class, along with the piecewise linear fit using training dataset. Open symbols (△) represents the training dataset. Closed symbols (▲) represents the test dataset. The inner tick-marks represent the projection of training dataset onto the x-axis.

0.117–0.524. This highlights that some of the observations in test dataset with low σ/σ_{TS} values are outside the range of σ/σ_{TS} range covered in training dataset. This is observed for all other compositions, where test dataset (t_f > 6,000 h) move towards lower σ/σ_{TS} values than the training dataset. Therefore, the coefficients such as k_1, u, and n may change with lower σ/σ_{TS} values. This is observed for **12Cr–1Mo–1W–Co–V–Cu** (▽) sub-class (Fig. 11), where k_1 and u changed with lower σ/σ_{TS} values. Fig. 11 also highlights the problem with using the mean value of Q_c^*, as 500 °C results does not fall on the estimated piecewise fit. This is more pronounced for Q_c', shown in Fig. 12. This indicates that either the mean Q_c^* / Q_c' estimates are wrong due to limited data for **12Cr–1Mo–1W–Co–V–Cu** (▽) sub-class, which also affects the estimation of change-point, or there is a need for different Q_c^* / Q_c' for different σ/σ_{TS} values.

The data does impose restrictions on the calculations of Q_c^* / Q_c', and may provide limitations when extending this technique to a new alloy design space with an optimized limited experimental observations. This can be evaluated in an hypothetical sense by reducing the amount of data used for the calculations of Q_c^* / Q_c'. In subsection 4.2 and subsection 4.3, all of the available data for each unique composition was used for calculating the Q_c^* / Q_c' values. A separate calculation for Q_c^* / Q_c' with restricted data, only t_f < 6,000 h tests, was able to evaluate Q_c^* for only 14 of 48 available compositions, and Q'_c for only 10 of 32 available compositions. The reasons for this are as follows: (1) data does not contain measurements at the same σ/σ_{TS} values and the availability of measurements at approximately the same σ/σ_{TS} values goes down when training data is restricted (t_f < 6,000 h), and (2) multiple constraints on the available data (described in subsection 4.2) further shrinks the available space for estimating Q_c^* / Q_c'. Although, these constraints can be fulfilled when designing experiments for new alloys (elaborated in subsection 5.5).

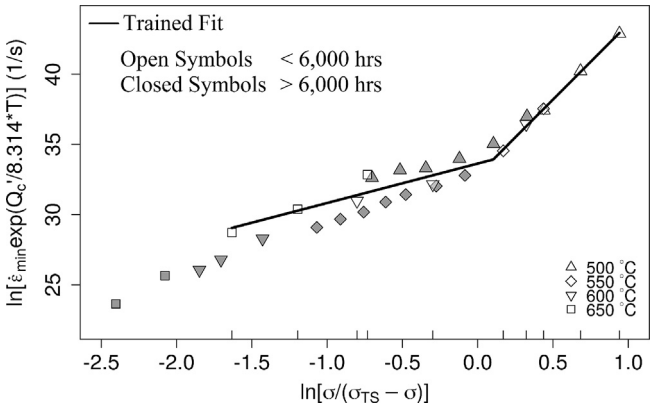

Fig. 12. Visualization of $\ln\{\dot{\varepsilon}_{min} \exp(Q'_c/RT)\}$ against $\ln[\sigma/(\sigma_{TS}-\sigma)]$ for the same composition as in Fig. 11, along with the piecewise linear fit using training dataset. Open symbols (△) represents the training dataset. Closed symbols (▲) represents the test dataset. The inner tick-marks represent the projection of training dataset onto the x-axis.

5.2. Dependence of Q_c^* / Q_c' on σ/σ_{TS}

Wilshire et al. [8,27] applied their method to 9–12 wt% **Cr** steel using a constant value of Q_c^*, although for austenitic steels [28] the authors used two different Q_c^* values: one for $\sigma > \sigma_{PS}$ (0.2% proof stress) and the other for $\sigma < \sigma_{PS}$. The data for the 9–12 wt% **Cr** martensitic steels studied herewith only contains the tests done at $\sigma < \sigma_{PS}$, therefore, no changes in Q_c^* would be expected based on previous work. Fig. 4 highlights that this is true for one unique composition where no strong dependence between Q_c^* and σ/σ_{TS} is observed. This does not prove to be a universal observation. For example, Fig. 13a shows an unique composition that exhibits a strong positive dependence between Q_c^* and σ/σ_{TS}, where the use of mean Q_c^* value overestimates at low σ/σ_{TS} and underestimates at high σ/σ_{TS} (Fig. 13b). The same observation is identified when

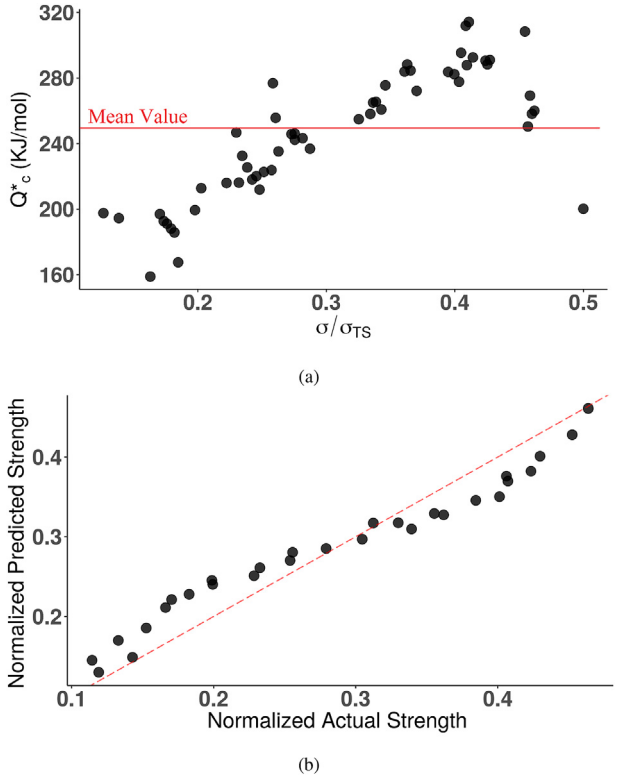

Fig. 13. (a) Visualization of Q_c^* as a function of σ/σ_{TS} for an unique composition from **12Cr–Mo-1.8W–V–Nb–Cu–B** (▲) sub-class, highlights an increase in Q_c^* with σ/σ_{TS}. (b) Visualization of predicted creep rupture strength against actual strength (both normalized with ultimate tensile strength (σ_{TS})) for the same composition using Wilshire et al. [8] method.

examining the Q'_c for this composition, consistent with a relationship between Q_c^* and Q'_c associated with the value of m. Alternatively, some compositions exhibit Q_c^* / Q'_c that decreases with σ/σ_{TS} (Fig. 14). The assumption that Q_c^* / Q'_c is independent of σ/σ_{TS} is false, which creates a feedback loop that can be observed in Figs. 13b and 14b.

We can classify the observed trends in the behavior of Q_c^* / $Q_c^{'}$ as a function of σ/σ_{TS} for each composition into three types: type *A*: where Q_c^* / $Q_c^{'}$ increases with σ/σ_{TS} (Fig. 13a), type *B*: where Q_c^* / $Q_c^{'}$ first increases and then decreases with σ/σ_{TS}, giving rise to a parabolic relationship (Fig. 5), and type *C*: where Q_c^* / Q'_c decreases with σ/σ_{TS} (Fig. 14a). These classifications result in a division of sub-classes into different types (i.e., *A*, *B*, and *C*) and are tabulated in Table 4.

One interpretation of the types can be the shift in parabolic peak location as a function of composition and processing parameters for σ/σ_{TS} values between 0.30 and 0.45. If the shift in the peak results in the three types of behavior, then, a physics-based model may be able describe why this shifts happens and it could be the next step for improving the contemporary methods. The differences in processing parameters for different types of compositions are discussed in the next section.

5.3. Role of processing parameters

The comparison of different sub-classes with respect to changes in composition and heat treatment provide limited insight into changes in Q_c^* / $Q_c^{'}$ with σ/σ_{TS} . The difference between short-term creep stability vs long-term creep stability is shown in Fig. 15. Sub-Fig. 15a and 15b highlight the effect of σ/σ_{TS} on t_f. For example, sub-figure (a,b) highlight sub-classes such as **12Cr–1Mo–1W–Co–V–Cu** (▽) which exhibit relatively good short-term creep strength although exhibit poor long-term strength (type *C*), this manifests as a sharp decrease in the derivative visualized in sub-figure (c). While sub-classes such as **12Cr–Mo-1.8W–V–Nb–Cu–B** (▲) retain their strength under long-term conditions (type *A*). This affect is explicitly shown in sub-Fig. 15c (for 600 °C), where a derivative of t_f with σ changes with t_f highlighting the differences between sub-classes. The comparison of Fig. 15a with Fig. 15b highlight sub-classes such as **9Cr-1.5Mo-1.3Co–V–Nb–B** (□), which lose their strength at higher test temperatures (type *C*) relative to sub-classes such as **9Cr–Mo-1.8W–V–Nb–B** (■) (type *A/B*). This affect is explicitly shown in sub-Fig. 15d, where a derivative of t_f with temperature (T) changes with t_f highlighting the differences between type C (blue) and type A/B (orange) sub-classes. The drop in creep strength with increased test temperature is strongly tied to low tempering temperature (or high dislocation density [29]) (Table 4).

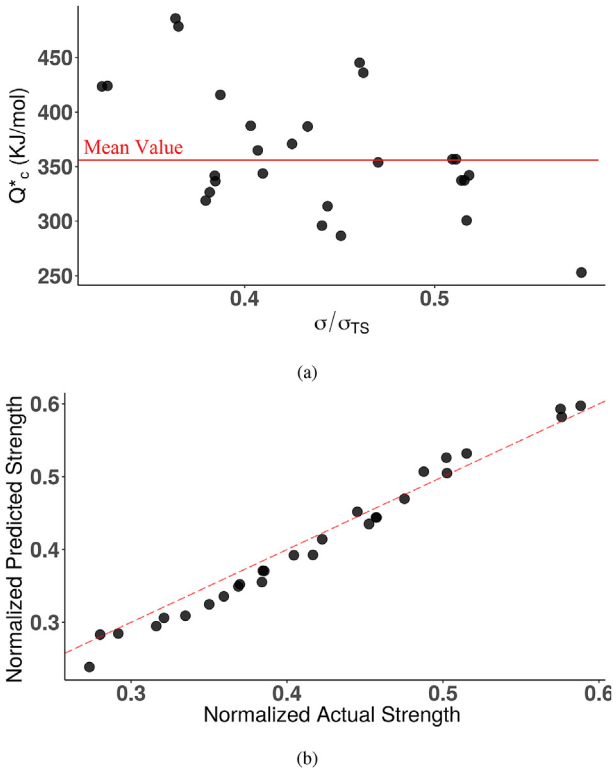

Fig. 14. Visualization of Q_c^* as a function of σ/σ_{TS} for an unique composition from **9Cr-1.5Mo-1.3Co–V–Nb–B** (□) sub-class, highlights a decrease in Q_c^* with σ/σ_{TS}. (b) Visualization of predicted creep rupture strength against actual strength (both normalized with ultimate tensile strength (σ_{TS})) for the same composition using Wilshire et al. [8] method.

Table 4
Classification of different sub-classes on the basis of the functional relationship between Q_c^* / Q'_c with σ/σ_{TS}, along with tempering temperature (represented as TPR). "–" in column "*Type*" represents that some of the unique compositions were not classified due to limited available Q_c^* / Q'_c values.

	Sub-Class	TPR	Type
(△)	12Cr	630–730	A(–)
(⋄)	9Cr–1Mo	720–860	C
(⊞)	9Cr–2Mo	800	C
(□)	9Cr-1.5Mo-1.3Co–V–Nb–B	700	C
(○)	10.5Cr–1Mo–1W–V–Nb	690	A/B
(▽)	12Cr–1Mo–1W–Co–V–Cu	630–660	C(–)
(⊕)	9Cr–1Mo–V–Nb	760–790	A
(■)	9Cr–Mo-1.8W–V–Nb–B	780	B
(•)	10.5Cr–Mo–2W–V–Nb–Cu–B	770	A/B
(▲)	12Cr–Mo-1.8W–V–Nb–Cu–B	790	A

For type *A* compositions, changes in creep deformation mechanism, from transgranular fracture mechanism in short-term creep vs brittle intergranular fracture in long-term creep has been observed [30], and this explains a decrease in activation energy with decrease in σ/σ_{TS}. Although, for type *C* compositions, a decrease in Q_c^* / $Q_c^{'}$ with an increase in σ/σ_{TS} is counterintuitive. These type *C* sub-classes exhibit a dramatic drop in strength with increased test temperature, which can be attributed to high initial dislocation density in **12Cr–1Mo–1W–Co–V–Cu** (▽) and **9Cr-1.5Mo-1.3Co–V–Nb–B** (□), and absence of pinning particles in **9Cr–1Mo** () and **9Cr–2Mo** (⊞). The exception to this observation is **12Cr** (△) sub-class, although the data for **12Cr** (△) sub-class was from limited range of test temperatures ($450 \leqslant T \leqslant 600$ °C).

5.4. Model comparison

A comparison of the different methodologies was presented in Table 3. The relatively similar RMSE and R^2 values indicate that one model is not significantly different from the other model in its ability to predict performance. The differences between the two methods stem from the values of m in Equation (1): Wilshire assumes m to be equal to one while Zhao method calculates m, requiring both t_f and $\dot{\varepsilon}_{min}$ values to be measured. As shown in Table 3, the need for both variable measures reduces the applicability of the Zhao method to the existing dataset. Further, to accurately measure $\dot{\varepsilon}_{min}$ requires additional experimental system complexity. For the family of 9–12 wt% **Cr** steels, the creep lifetimes are dominated by primary (constantly decreasing $\dot{\varepsilon}$) and ternary

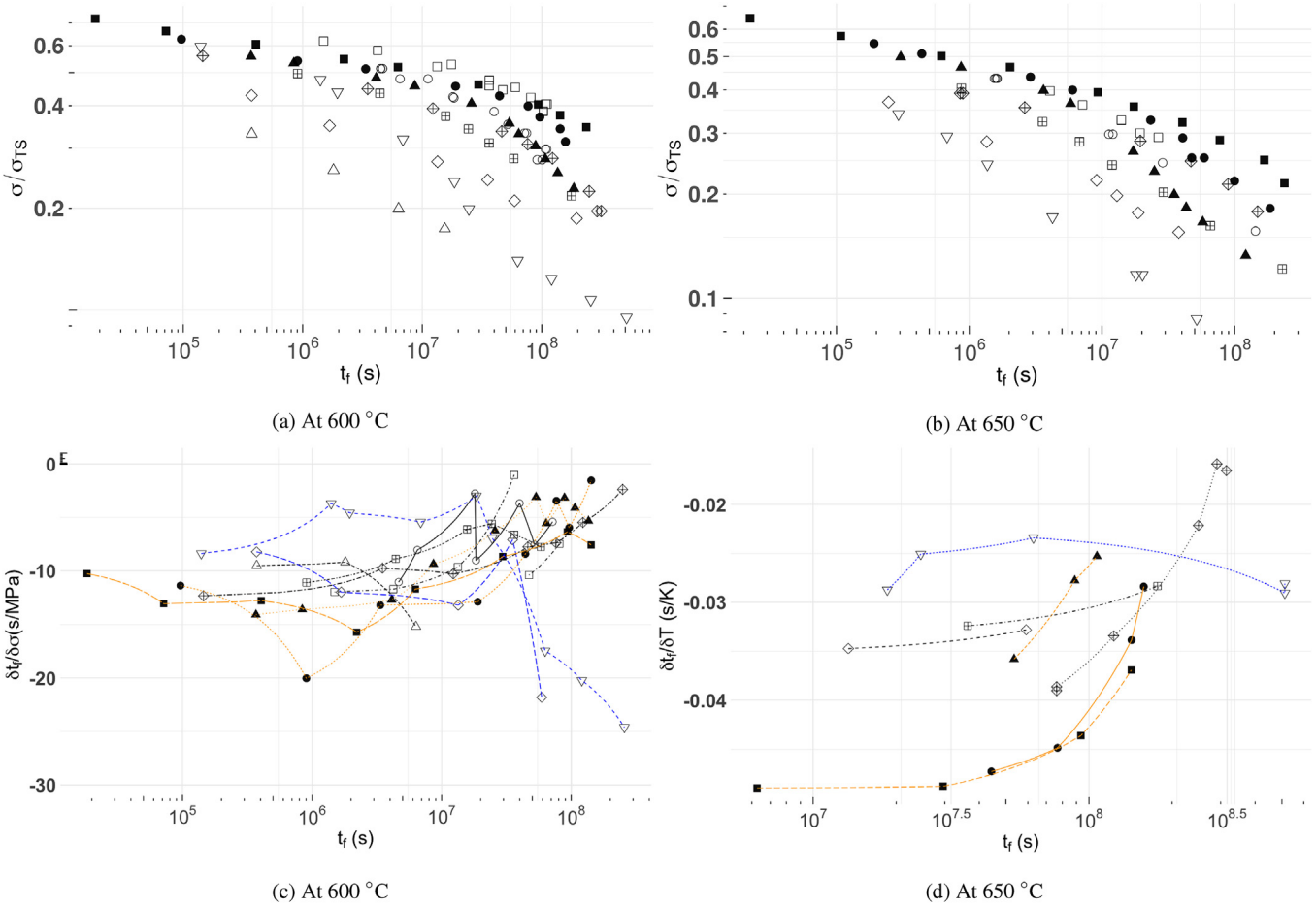

Fig. 15. (a,b) Visualization of t_f against (σ/σ_{TS}) for a single composition from each sub-class at (a) 600 °C, and (b) 650 °C. (c) Derivative of t_f with respect to σ at 600 °C. (Derivative at 650 °C is similar for each of the three types). (d) Derivative of t_f with respect to temperature (T) when going from 600 °C to 650 °C. (c,d) Blue curves highlight type C behavior, while orange curves highlight type A/B behavior. Different shapes represent sub-classes as shown in Table 1. (For interpretation of the references to colour in this figure legend, the reader is referred to the Web version of this article.)

creep regimes (constantly increasing $\dot{\varepsilon}$) [31]. Therefore, $\dot{\varepsilon}_{min}$ is only the transition point between the two regimes and not a extended regime in time (i.e., no secondary creep regime).

5.5. Design insights

The methods provide useful insights for the design of new martensitic steels even though the initial stated assumption of the two methods that "Q_c^* / Q'_c is independent of σ/σ_{TS}" is incorrect. The basic heuristics that can be developed here are as follows:

1. Design the experimental study protocols to cover a wide range of σ/σ_{TS} (e.g., 0.10–0.60) with multiple temperatures.
   - For example, if the design operating temperature is 650 °C, then cover at least a range of (550–750) °C with an interval of at most 25 °C.

The data density governs the uncertainty in the estimates of change-points for both methods. This does not mean to conduct experiments at all possible combinations of (σ, T), as experiments at low σ and low T from the range specified above may result in t_f > 6,000 h. On the other hand, experiments at high σ and high T may have a t_f of few hours. Both of these combinations do not reduce the uncertainty in the estimates of change-points as they are far-off. In general, creep test conditions, σ and T, follow an inverse relationship, where the optimal combination of the two is dictated by the creep life of the design test.

2. Evaluate Q_c^* / $Q_c^{'}$ for the entire range of (σ/σ_{TS}, T) to classify material as one of the types (i.e., *A*/*C*).
3. Make predictions using the mean Q_c^* / $Q_c^{'}$ value and evaluate σ/σ_{TS} for a desired creep lifetime (e.g., 10^5 h).
   - Mark predictions accordingly, i.e., if the material is type *A*, then predictions are overestimating the strength, and vice-versa for type *C*.
   - For type *B* compositions, both methods were able to predict strength by using the mean Q_c^* / $Q_c^{'}$ values, thereby validating the methodologies for this specific case.
4. Once evaluated, correct the σ/σ_{TS} estimates using a more appropriate Q_c^* / $Q_c^{'}$ value from step two.

The variation in Q_c^* / $Q_c^{'}$ with creep test conditions raises the question of whether these changes are related to changes in creep mechanism or are simply the result of data scatter/model failure. It also calls into question the physical interpretation of Q_c^* / $Q_c^{'}$ as the activation energy for creep. The elimination of the gradual decrease in n with σ, with a piecewise linear function for u/n with σ/σ_{TS} enables a researcher to predict creep rupture strength more reliably

than before by detecting these change-points. Although, attributing these change-points to mechanism changes without any microstructural evidence is questionable [32], and should be considered as simply the tools to improve model predictions.

Both methods rely on the dataset used for determination of constants and parameters, therefore, standard practices for the entire community should be developed to surmount the limitations highlighted by subsection 5.1 and subsection 5.2. The comparison of the two methods both highlights the strength of creep power law model for predicting long-term creep life using short-term data and also brings to question the physical interpretation of constants and parameters. Overall, both methods perform better than the traditional parametric methods as highlighted by Wilshire et al. [8] and Zhao et al. [9], and should continue to be used with caveat until better methods are available.

6. Conclusions

For new martensitic steels, validation of the long-term creep performance for a single composition can take 3–12 years using traditional methods, although, the contemporary methods explored in this study have the potential to reduce this timeline to an year. This work highlights the importance of a well constructed design space for estimating the constants/parameters for both methods to reliably predict the long-term strength. Several challenges highlighted in this study pushes the methods employed for the next phase of development. The modification of creep power law by Wilshire et al. [8] and Zhao et al. [9], and the comparison of the two methods presents the power laws as an empirical scheme which can be altered to improve predictions. This work questions the widely accepted notions about the physical parameters in creep power laws and its modified forms, and further challenges the stated assumptions while highlighting the importance of microstructural evidence.

Disclaimer

This project was funded by the Department of Energy, National Energy Technology Laboratory, an agency of the United States Government. Neither the United States Government nor any agency thereof, nor any of their employees, makes any warranty, expressed or implied, or assumes any legal liability or responsibility for the accuracy, completeness, or usefulness of any information, apparatus, product, or process disclosed, or represents that its use would not infringe privately owned rights. Reference herein to any specific commercial product, process, or service by trade name, trademark, manufacturer, or otherwise does not necessarily constitute or imply its endorsement, recommendation, or favoring by the United States Government or any agency thereof. The views and opinions of authors expressed herein do not necessarily state or reflect those of the United States Government or any agency thereof.

Acknowledgment

This project was funded by the Department of Energy, Grant DE-FE0028685, National Energy Technology Laboratory, an agency of the United States Government.

Appendix A. Function: Q_c^*

Written in R-language [25].

```
WilQ <- function(X) {
  X$ratio <- X$CS/X$UTS
  emptyDF <- X
  emptyDF <- emptyDF[0,]
  n <- nrow(X)
  min <- round(0.3*n)
  max <- 2*min
  colnm <- names(X)
  for (i in max:min) {
    group <- cut(X$ratio, i)
    tt <- split(X, group)
    for (j in 1:i) {
      temp <- as.data.frame(tt[j])
      if (nrow(temp) < 3) { next }
      colnames(temp) <- colnm
      fit <- lm(data = temp, log(RT) ~ I(1/CT.Temp))
      temp$Q <- fit$coefficients[2]*8.314/1000
      temp$AdjR2 <- summary(fit)$adj.r.squared
      temp$NoDT <- length(unique(temp$CT.Temp))
      temp$MR <- mean(temp$ratio)
      temp$RSD <- sd(temp$ratio)
      temp$n <- i
      emptyDF <- rbind(emptyDF,temp)
    }}
  if (nrow(emptyDF) < 2) { return(emptyDF) }
  emptyDF <- emptyDF[complete.cases(emptyDF$Q),]
  emptyDF <- emptyDF[complete.cases(emptyDF$AdjR2),]
  emptyDF <- subset(emptyDF, emptyDF$NoDT > 2)
  emptyDF <- subset(emptyDF, emptyDF$AdjR2 > 0.90)
  emptyDF <- emptyDF[!duplicated(emptyDF[,c(30:34)]),]
  library(fitdistrplus)
  fit <- fitdist(emptyDF$Q, distr = "norm", method = "mge")
  emptyDF <- emptyDF[emptyDF$Q > fit$estimate[1] -
   2*fit$estimate[2],]
  emptyDF <- emptyDF[emptyDF$Q < fit$estimate[1] +
   2*fit$estimate[2],]
  return(emptyDF)}
```

References

[1] D. Saha, The Rapidly Changing Landscape of Electricity Generation Mix across U.S. States, Sep. 2017. http://knowledgecenter.csg.org/content/rapidly-changing-landscape-electricity-generation-mix-across-us-states?nopaging=1.

[2] J. Shingledecker, R. Purgert, P. Rawls, Current status of the US DOE/OCDO A-USC materials technology research and development program, in: Proceeding the 7th International Conference on Advances in Materials Technology for Fossil Power Plants (2013. 10), 2013, pp. 41–52. https://www.asminternational.org/search/-/journal_content/56/10192/05440G/PUBLICATION.

[3] F.R. LARSON, J. Miller, A time temperature relationship for rupture and creep stress, Trans. ASME 74 (1952) 765–771. http://ci.nii.ac.jp/naid/10029483297/.

[4] S.S. Manson, A.M. Haferd, A linear time-temperature relation for extrapolation of creep and stress-rupture data. http://ntrs.nasa.gov/search.jsp?R=19930083803.

[5] F.T. Furillo, S. Purushothaman, J.K. Tien, Understanding the larson-miller parameter, Scr. Metall. 11 (6) (1977) 493–496. http://www.sciencedirect.com/science/article/pii/0036974877901648.

[6] S.S. Manson, C.R. Ensign, Interpolation and Extrapolation of Creep Rupture Data by the Minimum Commitment Method. Part 3: Analysis of Multiheats, 26-29 Jun. 1978, 1978. https://ntrs.nasa.gov/search.jsp?R=19780015530.

[7] I.A. Shibli, S.R. Holdsworth, G. Merckling, Creep and Fracture in High Temperature Components: Design and Life Assessment Issues, DEStech Publications, Inc, 2005 google-Books-ID: uyE_Ry3NHNEC.

[8] B. Wilshire, P.J. Scharning, A new methodology for analysis of creep and creep fracture data for 9–12% chromium steels, Int. Mater. Rev. 53 (2) (2008) 91–104. https://doi.org/10.1179/174328008X254349.
[9] Y.R. Zhao, H.P. Yao, X.L. Song, J. Jia, Z.D. Xiang, On the physical models for predicting the long-term creep strengths and lifetimes of modified 9cr-1mo steel, J. Alloy. Comp. 726 (2017) 1246–1254. http://www.sciencedirect.com/science/article/pii/S0925838817328104.
[10] K. Yadi, NIMS Creep Data Sheet (JIS SUS 403-B, 12cr, Bar), Tech. Rep. 13B, NIMS, Tokyo, 1994.
[11] H. Irie, NIMS Creep Data Sheet (JIS STBA 26, 9cr-1mo, Tube), Tech. Rep. 19B, NIMS, Tsukuba, 1997.
[12] H. Irie, NIMS Creep Data Sheet (1cr-0.5mo-0.25v and 12cr-1mo-1w-0.25v, Bolting Material), Tech. Rep. 44, NIMS, Tsukuba, 1997.
[13] H. Irie, NIMS Creep Data Sheet (JIS SUH 616-B, 12cr-1mo-1w-0.3v, Bar), Tech. Rep. 10B, NIMS, Tsukuba, 1998.
[14] S. Matsuoka, NIMS Creep Data Sheet (KA-STBA 27, 9cr-2mo, Tube), Tech. Rep. 46A, NIMS, Tsukuba, 2005.
[15] NIMS Creep Data Sheet, Tech. Rep. 48A, NIMS, Japan, 2012.
[16] NIMS Creep Data Sheet (KA-SUS 410 J3, 12cr-2w-0.4mo-1cu-Nb-V), Tech. Rep. 51A, NIMS, Japan, 2013.
[17] NIMS Creep Data Sheet (KA-SUS 410j3 DTB, 12cr-2w-0.4mo-1cu-Nb-V (Tube)), Tech. Rep. 52A, NIMS, Japan, 2013.
[18] NIMS Creep Data Sheet (9cr-1mo-V-Nb), Tech. Rep. 43A, NIMS, Japan, 2014.
[19] F.C. Monkman, N.J. Grant, An empirical relationship between rupture life and minimum creep rate in creep rupture tests, Proc. ASTM 56 (1956) 593–620. https://ci.nii.ac.jp/naid/10006401917/.
[20] M.E. Kassner, Chapter 2 - five-power-law creep, in: Fundamentals of Creep in Metals and Alloys, third ed., Butterworth-Heinemann, Boston, 2015, pp. 7–102. http://www.sciencedirect.com/science/article/pii/B9780080994277000025.
[21] V.M. Muggeo, , segmented: an r package to fit regression models with broken-line relationships, R. News 8 (1) (2008) 20–25. https://cran.r-project.org/doc/Rnews/.
[22] V.M.R. Muggeo, Estimating regression models with unknown break-points, Stat. Med. 22 (19) (2003) 3055–3071. https://onlinelibrary.wiley.com/doi/abs/10.1002/sim.1545.
[23] G. James, D. Witten, T. Hastie, R. Tibshirani, An Introduction to Statistical Learning, Vol. 103 of Springer Texts in Statistics, Springer, New York, New York, NY, 2013. http://link.springer.com/10.1007/978-1-4614-7138-7.
[24] F. Masuyama, History of power plants and progress in heat resistant steels, ISIJ Int. 41 (6) (2001) 612–625. https://www.jstage.jst.go.jp/article/isijinternational1989/41/6/41_6_612/_article.
[25] R Core Team, R: A Language and Environment for Statistical Computing, R Foundation for Statistical Computing, Vienna, Austria, 2017. https://www.R-project.org/.
[26] M.L. Delignette-Muller, C. Dutang, fitdistrplus: an R package for fitting distributions, J. Stat. Softw. 64 (4) (2015) 1–34. http://www.jstatsoft.org/v64/i04/.
[27] B. Wilshire, P.J. Scharning, Long-term creep life prediction for a high chromium steel, Scr. Mater. 56 (8) (2007) 701–704. http://www.sciencedirect.com/science/article/pii/S1359646207000231.
[28] M.T. Whittaker, M. Evans, B. Wilshire, Long-term creep data prediction for type 316h stainless steel, Mater. Sci. Eng. (2012) 145–150. A 552, http://www.sciencedirect.com/science/article/pii/S0921509312007150.
[29] P. Yan, Z. Liu, H. Bao, Y. Weng, W. Liu, Effect of tempering temperature on the toughness of 9cr–3w–3co martensitic heat resistant steel, Mater. Des. 54 (2014) 874–879, 1980-2015, http://www.sciencedirect.com/science/article/pii/S0261306913008698.
[30] K. Maruyama, K. Yoshimi, Influence of data analysis method and allowable stress criterion on allowable stress of Gr.122 heat resistant steel, J. Press. Vessel Technol. 129 (3) (2006) 449–453. https://doi.org/10.1115/1.2748825.
[31] F. Abe, Precipitate design for creep strengthening of 9% Cr tempered martensitic steel for ultra-supercritical power plants, Sci. Technol. Adv. Mater. 9 (1) (2008), 013002. http://stacks.iop.org/1468-6996/9/i=1/a=013002.
[32] V. Gray, M. Whittaker, The changing constants of creep: a letter on region splitting in creep lifing, Mater. Sci. Eng. (2015) 96–102. A 632, http://www.sciencedirect.com/science/article/pii/S0921509315001768.